

A Photometric Investigation of the GRB970228 Afterglow and the Associated Nebulosity

Francisco J. Castander and Donald Q. Lamb

Department of Astronomy and Astrophysics, University of Chicago,
5640 S Ellis Ave, Chicago, IL 60637

ABSTRACT

We carefully analyze the WFPC2 and STIS images of GRB970228. We measure magnitudes for the GRB970228 point source component in the WFPC2 images of $V = 26.20^{+0.14}_{-0.13}$, $I_c = 23.94^{+0.10}_{-0.09}$ and $V = 26.52^{+0.16}_{-0.18}$, $I_c = 24.31^{+0.15}_{-0.11}$ on March 26 and April 7, respectively; and $R_c = 27.09^{+0.14}_{-0.14}$ on September 4 in the STIS image. For the extended component, we measure magnitudes of $R_c = 25.48^{+0.22}_{-0.20}$ in the combined WFPC2 images and $R_c = 25.54^{+0.33}_{-0.22}$ in the STIS image, which are consistent with no variation. This value is fainter than previously reported (Galama et al. 1998) and modifies the previously assumed magnitudes for the optical transient when it faded to a level where the extended source component contribution was not negligible, alleviating the discrepancy to a power-law temporal behavior. We also measure a color of $V_{606} - I_{814} = -0.18^{+0.51}_{-0.61}$ for the extended source component. Taking into account the extinction measured in this field (Castander & Lamb 1998), this color implies that the extended source is most likely a galaxy with ongoing star formation.

Subject headings: gamma rays: bursts — galaxy: starbursts

1. Introduction

On 1997 February 28 the Gamma-Ray Burst Monitor aboard the BeppoSAX satellite detected a gamma-ray burst (GRB) and its Wide Field Camera (WFC) instrument imaged it. A few hours later the BeppoSAX team disseminated a positional error circle of 3' radius to the astronomical community (Costa et al. 1997a). Eight hours after the burst, and again three days later, the BeppoSAX Narrow Field Instrument observed this error circle. These observations revealed a rapidly fading X-ray source at a position that was consistent with both the WFC position for this event and with the Inter Planetary Network (IPN) annulus calculated from the time-of-flight between Ulysses and BeppoSAX spacecrafts (Costa et al. 1997b). ASCA (Yoshida et al. 1997) and ROSAT (Frontera et al. 1997, 1998b) observations showed that the X-ray source continued to fade over the following two weeks, and provided a 10" radius position for this source.

Ten days after the burst, Groot et al. (1997a) announced the detection of an optical fading source ($V = 21.3$) which turned out to be the first optical counterpart detected of a GRB. Two days

later Groot et al. (1998b) and Metzger et al. (1997a) reported the presence of an extended source ($R = 23.8$) at a position consistent with that of the optical transient. Groot et al. (1997b) and van Paradjis et al. (1997) claimed that the extended source was the host galaxy, but a subsequent ground based optical observation indicated that the extended source had faded (Metzger et al. 1997b). Once the position of the afterglow was firmly established, early observations were revisited and new ones taken. This new detections provide a better sampling of the optical afterglow behavior (Klose et al. 1997; Margon et al. 1997; Soifer et al. 1997; Metzger et al. 1997b; Pedichini et al. 1997a; Djorgovski et al. 1997). The HST Wide Field and Planetary Camera 2 (WFPC2) provided another breakthrough in the follow up of the GRB970228 optical afterglow. Observations made on March 26 revealed two components: one consistent with being a point source and the other an extended source (Sahu et al. 1997a). Further observations on April 7 showed that the point source was fading while the extended source remained unchanged within the observational uncertainties (Sahu et al. 1997b). The GRB970228 optical afterglow was observed again with HST using the Space Telescope Imaging Spectrograph (STIS) on September 4 (Fruchter et al. 1997). These new images corroborated the earlier observations: a point-like fading optical source and an extended source, which has been claimed to be the host galaxy.

Reichart (1997) and Wijers et al. (1997) discussed early observations of GRB970228 in the context of theoretical models. They found that the gamma-ray burst afterglow behavior was consistent with the expectations of relativistic fireball models. Later, Galama et al. (1998) (revising and updating Galama et al. (1997)) compiled the most relevant photometric measurements of GRB970228, converting them into a single photometric band when necessary and subtracting the contribution of the extended source component. They fit the optical transient temporal evolution to a power-law with $\alpha = -1.10 \pm 0.04$ ($\chi_r^2 = 2.3$, 9 d.o.f.).

In a companion paper (Castander & Lamb 1998; hereafter CL98), we have determined the galactic extinction towards GRB970228, performing a careful analysis of the publicly available observations. Here we focus on the photometric properties of the point-like and extended components revealed in the HST observations, and analyze their magnitudes taking into account the measured extinction. In §2 we detail our analysis of the WFPC2 and STIS HST images. In §3 we discuss our results and in §4 we summarize our conclusions.

2. HST photometry

The HST images of the GRB970228 afterglow, given their superior spatial resolution compared to ground-based imaging, provided a startling result. On March 26 the WFPC2 images showed two components: a point-like and an extended source (Sahu et al. 1997a), whose centers were approximately $0.4''$ apart. In further observations on April 7, the point source component was observed to fade while the magnitude of the extended component was consistent with no variation within the measured errors (Sahu et al. 1997b; Sahu et al. 1997c). On September 4, the HST STIS instrument imaged the GRB970228 field. The point source showed further dimming while the

extended component showed no appreciable variation, after correction of the magnitudes reported by Sahu et al. (1997c) (Fruchter et al. 1997; Fruchter et al. 1998).

Given the outstanding importance of these measurements, we have undertaken on a careful reanalysis of the HST photometry to discern the nature of the GRB970228 optical counterpart in conjunction with the extinction values measured in CL98.

2.1. Wide Field and Planetary Camera 2 observations

GRB970228 was observed by the HST WFC2 on March 26th and April 7th. In both observations the optical counterpart was centered in the middle of the PC1 CCD, but there was a 2.40 deg difference in rotation angle between the first and second observations. At both epochs, four exposures were taken in the F606W filter and two exposures in the F814W filter, totalling 4700 and 2400 seconds, respectively (Sahu et al. 1997c).

In CL98 we analyzed the WFPC2 images to obtain number counts and described the reduction process performed using standard tasks. However, in order to accurately estimate the magnitudes and especially the errors of the objects in the GRB position which consist of a faint point source coincident with an extended faint surface brightness component, we developed some specific software to carry out the photometry.

Our procedure was the following. We combined the observations in a similar fashion as standard software does, eliminating cosmic rays by sigma clipping with three different threshold passes cutting at 8, 5 and 3 sigma¹ and also eliminating hot pixels masked out by the standard reduction pipeline. After combining the images, we ended up with four values for every pixel: 1) total counts of non-rejected pixels; 2) number of valid non-rejected pixels used; 3) total exposure of combined pixels used; and 4) error on the total counts in 1), estimated as the square root of the counts plus the contribution of the read-out noise.

We then calculated the centroid position of objects S1, S2 (the brightest stars in the PC1 CCD at 2.9" West and 16.8" East from the GRB respectively; see Figure 2 of CL98 for a finding chart) and the point and extended source components of the GRB. The centroids were obtained using the CENTER task within IRAF with the centroid algorithm. Centering in these computed positions, the sky was estimated from circular annuli around each object. For each object the sky was computed from 30 annuli differing in their outer radii. A different sky value with its associated variance was computed for pixels that had different number of rejections in the cosmic ray and hot pixel rejection process. For the F606W filter the combination was done with four images and typically (there is a slight difference for each object) there were pixels with no rejections ($\sim 89\%$), with one rejection ($\sim 10\%$) and two rejections ($\sim 1\%$). For the F814W filter the combination

¹All four sets of images were clipped at these levels except the F814W 970407 set, which presented a higher background level and was clipped at lower sigma threshold (8,5,2.5 sigma).

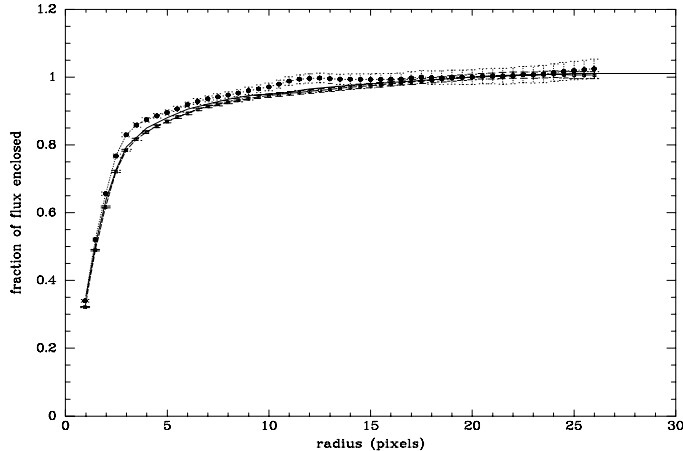


Fig. 1.— Point spread function for star S1 (dotted line and solid circles), S2 (dashed line and open squares) in the combined F606W WFPC2 images taken on March 26 and that defined by Holtzman et al. (1995a) (solid line).

was done with two images and typically there were pixels with no rejections ($\sim 95\%$) and with one rejection ($\sim 5\%$). For every one of the 30 annuli we plotted the values of the median and the standard deviation for each pixel with the same number of rejections. We obtained the final sky value and its variance for each number of pixel rejections visually from the plot. Our visual choice, nevertheless, was similar to the median of the 30 annuli medians and the median of the 30 annuli standard deviations. Subsequently, we calculated aperture photometry in circular and elliptical (only for the extended component of the GRB) apertures at radii and semimajor axes varying from 1 to 30 pixels² around each object. We added the pixels values (and fractional pixel values at the edges) within the apertures, subtracting the sky values for the appropriate number of pixel rejections, taking into account the error of both counts and sky, and normalizing to a common exposure. Each aperture had therefore a properly computed count flux and error.

We used stars S1 and S2 to define the point spread function (PSF). Figure 1 shows the normalized counts for both stars at all apertures used together with the approximate encircled energy curve for the PC1 given by Holtzman et al. (1995a) that serves as comparison.

Table 1 summarizes our photometric measurements. We first analyzed the point source component. We measured its magnitude minimizing the χ^2 of the fit of the inner radial bin counts of the point source to the same bins for stars S1, S2 and the PC1 PSF, where the normalization of the stars is the free parameter being fit. We used five bins: the first one corresponds to the counts in a 1 pixel radius circle and the other four, to the counts in successive concentric circular annuli of 0.5 pixels width. That is, we fit the inner 3.0 radius circle counts to three model PSFs. The extended

²Pixel scale: 0.0455"/pixel

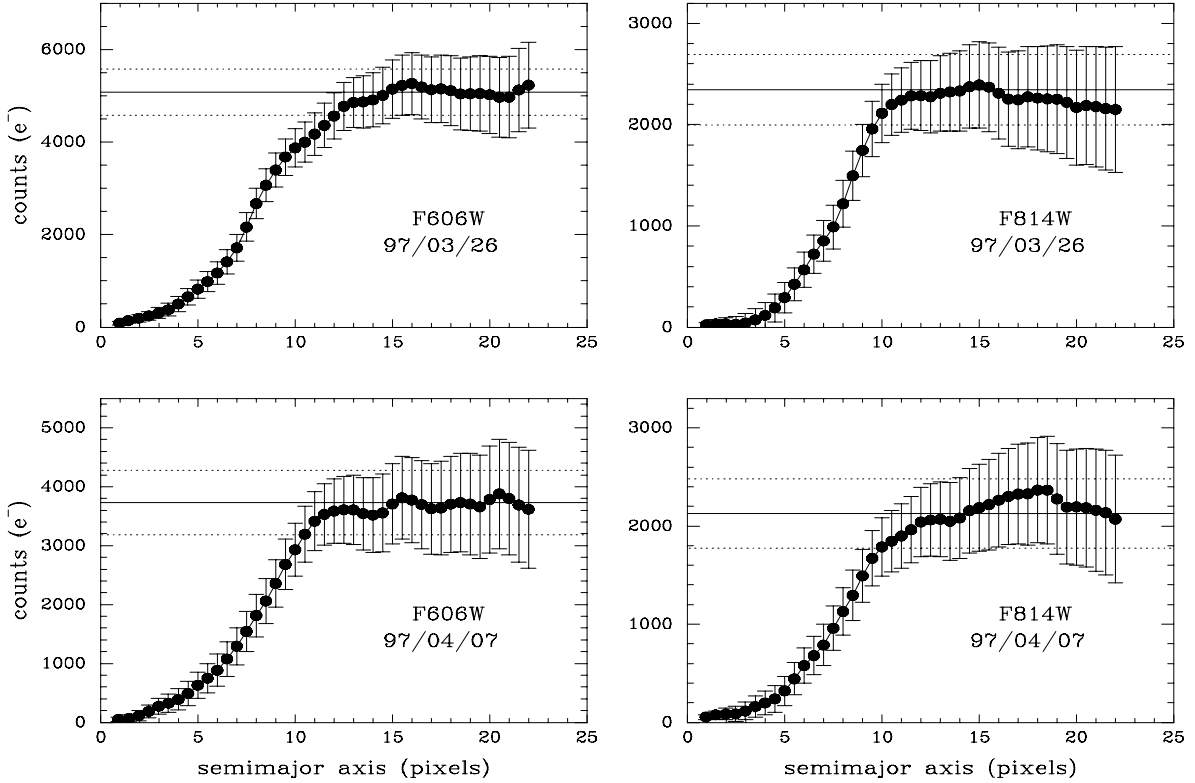


Fig. 2.— Enclosed counts as a function of semimajor axis for the extended+point components in the WFPC2 images. The solid line illustrates the value adopted and the dashed lines its error.

component was measured in circular and elliptical apertures, beginning at the estimated centroid and extended out to 30 pixels radius/semimajor axis. Then we plotted the counts enclosed in every aperture as a function of aperture radius/semimajor axis and assigned the counts of the extended and point components to the value at which the counts remained approximately unchanged with increasing radius. We estimated the error as the error in the aperture where the counts started to flatten, $a \simeq 12$ pixels (see Figure 2). We found that the exact choice of the centroid and ellipticity did not affect our measurements. These measured counts and errors correspond to both the point and extended components, as both lie within the apertures where the counts flatten. Then we calculated the extended component magnitude by subtracting the point source contribution to the total counts. Once we had this first estimation of the extended source, we then estimated the extended source contribution to the pixels where the point component was measured and redid the χ^2 fit to the point source including this contribution. Having obtained this new value and the previously measured point+extended counts, we again calculated the extended component magnitude and its error.

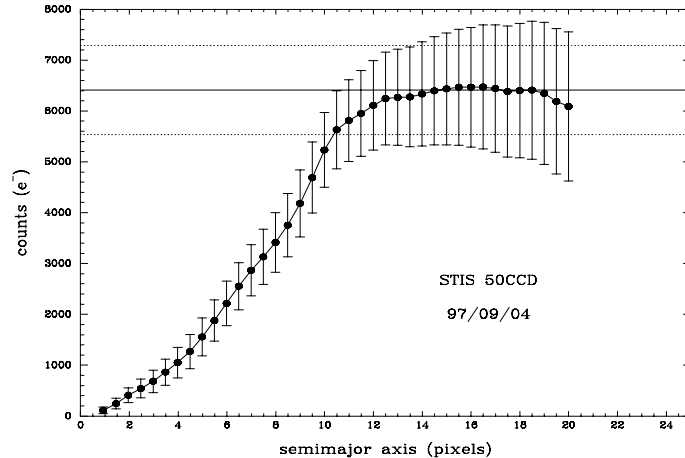


Fig. 3.— Enclosed counts as a function of semimajor axis for the extended+point components in the STIS image. The solid line illustrates the value adopted and the dashed lines its error.

2.2. Space Telescope Imaging Spectrograph observations

On September 4 the STIS instrument onboard HST imaged the GRB970228 from 4.6601 to 4.7657 UT. Two exposures of 575s each were taken in the clear aperture (50CCD) mode at each of four dithered positions for a total exposure time of 4600s. The dithered positions were at 0.125" SW, 0.125" SE and 0.250" S offsets from the first image for the second, third and fourth images respectively. We retrieved the pipeline-processed images from the HST archive once they became public almost two months after being taken. We reduced them in a similar fashion as was done with the WFPC2 images, although in this case we had to shift the images to correct for the dithering, which required some rebinning, as the offsets were not done at integer pixels for all four images. We again ended up with an image having four values per pixel: 1) total number of non-rejected counts; 2) number of valid non-rejected pixels used; 3) total non-rejected exposure; and 4) error on the total counts.

We then proceeded as we had with the WFPC2 images, obtaining the sky value and variance for every object, and the number of rejected pixels. In the STIS images typically 96% of the pixels had no rejections, 4% one rejection and less than 0.1% had two rejections. Table 2 summarizes our photometry. Magnitudes were computed as for the WFPC2 images.

3. Discussion

We have undertaken an effort to determine the photometry of the optical and extended components of the GRB970228 optical counterpart, as observed by the HST WFPC2 and STIS instruments. We have tried to perform the best magnitude determination with a rigorous treatment

of the errors. As described in the previous section, we started by combining the original pipeline processed images, retaining the rejection information to propagate it into our error analysis. Our subsequent sky subtraction was based on a multi-aperture estimation that takes into account the number of rejected pixels in the combination process. Although the sky varies depending on the exact area used to estimate it, our multi-aperture estimation reduces problems that could arise from selecting an area with deviant values. Our error also takes into account the variance of the sky estimation due to the selected area. Although the fraction of rejected pixels per unit area is relatively stable throughout all regions of the images studied, we also apply a different sky correction depending on the number of rejected pixels.

We have chosen to determine the magnitude of the point source component by fitting the inner counts radial profile to the PSF. We use the radial profile within the inner 3.0 pixels (0.136") for the WFPC2 images and the inner 2.0 pixels (0.1") for the STIS images, taking into account in a second phase the contribution of the extended component as well. The radius used in the STIS analysis was smaller in an attempt to reduce the uncertainties of the contribution of the extended source, as the point source is significantly fainter in this observation. Once the fit is done, we extrapolate the PSF profile to obtain the total counts (see previous section for further details). We believe that this is the best procedure to obtain the point component magnitude and its error. The method should give results that are, however, similar to obtaining aperture photometry and applying a correction factor for that aperture to get the total magnitudes. Our method is essentially the same, but performed for several radii. We use the two brightest stars in the field, S1 and S2, and the Holtzman et al. (1995a) and Robinson et al. (1997) determination of the PSF for WFPC2 and STIS, respectively, as the model PSF to which the point component data was fit. Table 3 provides the reduced χ^2/ν values for the different filters and epochs of the observations. Fits are acceptable in all cases except for the April F606W and the STIS images. In both cases the radial count distribution profile is more extended than that of the stars and model PSF. Our choice of measuring method by profile fitting is not optimal in these two cases, but is more accurate than single aperture photometry. The outermost radius we use in the fits encloses approximately 80% and 65% of the counts (WFPC2 and STIS images respectively), so our extrapolation of the profile only contributes at most $\sim 35\%$ of the total counts. If we change the outermost radius in the fits our extrapolated total counts do not vary appreciably. Only in the two cases where the PSF fit is poor is the variation somewhat larger. Finally, we would like to emphasize that we include an estimated contribution of the extended component in the pixels measured when performing the fit.

We estimate the total counts of the extended+point components by elliptical aperture photometry (see previous section). We increase the semimajor axis until the counts flatten with radius. Due to different centroiding, the counts do not flatten at the same semimajor axis value in all cases. In Figure 2 we can see how the number of counts levels off and remains approximately constant with increasing semimajor axis for the F606W filter, providing a relatively safe count estimation. For the F814W filter, however, the number of counts still varies somewhat at large radii. In this case the image combination was performed only with two images and the cosmic ray/hot pixel removal

is more difficult. For example, if we had chosen a lower threshold rejection in the combination process, the increase in the number of counts in the F814W 97/04/07 image at semimajor axis values from 15 to 18 pixels disappears, as this feature is due to a count excess present in only one of the images that was not rejected properly with the threshold used.

With the measured counts and exposure times we compute ST magnitudes³ for the point and extended components using the header keywords PHOTFLAM and PHOTZPT in the WFPC2 images (Table 1). For the STIS image we present count rates (Table 2), since the STIS ST magnitude in open mode is not very useful, given that an assumed spectrum is required to convert STIS 50CCD count rates to other broad band filter magnitudes. In order to compare the HST observations with other ground-based magnitude measurements, we convert our values to Johnson-Cousins magnitudes. Instead of using color transformation relations (Holtzman et al. 1995b), we fit a spectrum to the observed colors, convolving the spectrum with the filter responses. We then compute the expected magnitude in a particular filter with the spectral fit.

We fit a power-law spectrum for the point source and a galaxy spectrum for the extended component. In both cases we assume a foreground $R_V = 3.1$ extinction law of $A_V = 1.19$ (CL98) and no intrinsic reddening at the source. Obviously, the reddening assumed for the point source component is irrelevant, since the extinction law behaves approximately as a power law in the wavelength range used and the only effect caused is a change in the power-law slope of the fit. The point source spectrum is fit at both epochs for the WFPC2 images. The best-fit power-law indexes are: 1.17 and 1.06 for March 26 and April 7, respectively. To compute standard filter magnitudes for the point source from the STIS number counts we assume an $A_V = 1.19$ extinguished power-law spectrum that gives the mean of the color between the two WFPC2 observations, $V_{606} - I_{814} = 0.70$. The errors in the magnitudes come from varying the power-law indexes to allow for all possible values of the observed $V_{606} - I_{814}$ color in the WFPC2. We assumed that there was no color evolution for the point source component from the March 26 and April 7 WFPC2 observations to the September 4 STIS observations.

We have combined the two WFPC2 observations to provide the best magnitudes and errors for the extended component. We add the measured counts, weighting them by their relative errors. With them, we compute the resulting magnitudes and errors. We obtain $V_{606} = 26.03_{-0.16}^{+0.19}$ and $I_{814} = 26.21_{-0.33}^{+0.45}$. For the extended source we assume a galaxy spectrum to convert from the combined HST measurements to standard filters magnitudes. There are several galaxy templates at different redshifts that reproduce the observed colors. We choose an $A_V = 1.19$ extinguished spectrum of a starburst galaxy with constant star formation observed at $z = 1.46$, 1 Gyr after the onset of the burst (see below) to convert from the best-fitting magnitudes in the WFPC2 filters to Johnson-Cousins'. To allow for the possible spectral differences allowed by the observed color errors, we compute the color transformation for a variety of synthetic galaxy spectra that bracket

³All magnitudes that we quote for the GRB97028 point and extended components are in the ST system for the WFPC2 filters and in the Vega system for standard Johnson-Cousins filters

the measured error in the $V_{606} - I_{814}$ color. Therefore, the errors in the standard filters include the measured color error plus the contribution due to the different spectral energy distributions (SED) allowed. Our search of SEDs compatible with the observed colors has been extensive but by no means complete. Nevertheless, we believe that the estimated contribution to the error due to the allowed SEDs is appropriate. In the STIS case, we proceed in a similar fashion to compute magnitudes from count rates. As for the WFPC2 case, the best-fitting value is obtained with a spectrum of a 1 Gyr old burst of star formation observed at $z = 1.46$; and its error, from the combination of the contribution due to the error in the measured count rate and the contribution due to the allowed SEDs as determined by the measured colors in the WFPC2 observations. Tables 1 and 2 present our measured magnitudes.

Once the magnitudes of point and extended sources have been measured, what can we learn about them? For the point-source component, our magnitudes are consistent with those measured by Sahu et al. (1997c) in the V band but are 0.3 magnitudes brighter in I_c . Overall, our computed color ($V - I_c = 2.23$) is redder than that of Sahu et al ($V - I_c = 1.85$). We have assumed a power-law spectrum to convert between ST and standard filter magnitudes (see above). Our magnitudes do not appreciably change if we were to use instead the photometric transformation of Holtzman et al. (1995b). Our R_c magnitudes are, nevertheless, almost identical to those computed by Galama et al. (1997) from Sahu et al's data. We are unable to comment on the discrepancy of the I_c magnitudes as Sahu et al. (1997c) do not provide enough details for a comparison. In the STIS image we measure a count rate of $0.232_{-0.022}^{+0.023}$ for the point source. Our estimated V and R_c magnitudes are consistent within the errors with those measured by Fruchter et al. (1998) and Galama et al. (1998). Fruchter et al. (1998) measure $V = 28.0 \pm 0.25$ while we get $V = 28.10_{-0.23}^{+0.24}$. The 0.1 mag difference in our best values could be entirely due to the spectrum assumed to convert from STIS counts to magnitudes. In the R_c filter, our measurement, $R_c = 27.09_{-0.23}^{+0.24}$, is more discordant to that of Galama et al. (1998), $R_c = 27.25 \pm 0.27$. In this case, the conversion between STIS counts and R_c magnitudes is less dependent on the assumed spectrum (as can be seen in Table 2, where the errors bars are smaller for this filter) and the 0.16 mags difference in our best values is probably due to different measured count rates. There are indications that the OT is becoming redder in its evolution (e.g., Galama et al. 1998). The spectrum assumed to convert count rates to magnitudes has not taken into account this possibility. However, the effect should be small and should not affect our R_c magnitude appreciably.

For the extended component, our measured magnitudes for the WFPC2 and STIS images agree remarkably well. To convert from STIS count rate to magnitudes, we have assumed a spectrum that fits the WFPC2 colors. That is the reason why the colors for the extended component are the same in the WFPC2 and STIS images (Tables 1 and 2). Compared to previous work, our V magnitudes agree within the errors with those of Fruchter et al. (1997) and Fruchter et al. (1998) ($V = 25.6 \pm 0.25$ and $V = 25.7 \pm 0.25$ for WFPC2 and STIS respectively). However, we disagree with the $R_c = 25.0 \pm 0.3$ magnitude quoted by Galama et al. (1998). Combining the WFPC2 and STIS magnitudes we obtain $R_c = 25.51_{-0.15}^{+0.18}$. This magnitude would imply a slightly different temporal

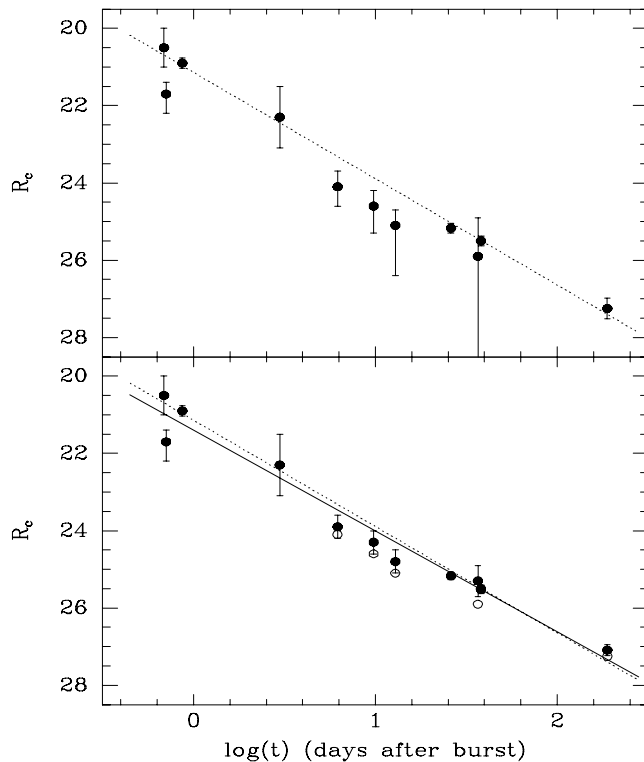


Fig. 4.— The R_c light curve of GRB970228. Top Panel: light curve by Galama et al. (1998) with their power-law fit ($\alpha = -1.10$, dotted line). Bottom panel: light curve with OT magnitudes revised with our value of the extended component magnitude with our best power-law fit ($\alpha = -1.04$, solid line). For comparison, the Galama et al's points are plotted as open circles, their power-law fit as dotted lines.

behavior for the OT than that reported by Galama and collaborators, because they overcorrected for the contribution of the extended component when the OT faded to fluxes comparable to that of the extended component. Figure 4 shows the R_c light curve of Galama et al. (1998) (top panel) along with our revised light curve (bottom panel). In the bottom panel we also plot the Galama et al's points as open circles to compare the difference that the revised extended component magnitude has on the OT magnitudes. We plot both curves in order to compare error bars as well. The new revised OT magnitudes produce a better fit to a power-law behavior than before at late epochs (after the first week). If we consider only the last 7 photometric points, that is, the evolution after March 06, we obtain a power-law temporal decay of $\alpha = -0.86 \pm 0.06$ ($\chi^2/\nu = 0.27$, 5 d.o.f). The same points with the Galama and collaborators values would give $\alpha = -0.82 \pm 0.10$ ($\chi^2/\nu = 0.71$, 5 d.o.f). However, considering all the photometric points we obtain $\alpha = -1.04 \pm 0.03$ ($\chi^2/\nu = 2.49$, 9 d.o.f.; note the overly small errors in the slope due to the poor χ^2 fit) .vs. the $\alpha = -1.10 \pm 0.04$ ($\chi^2/\nu = 2.3$, 9 d.o.f) of Galama et al. Therefore, it appears that the temporal decay is slowing

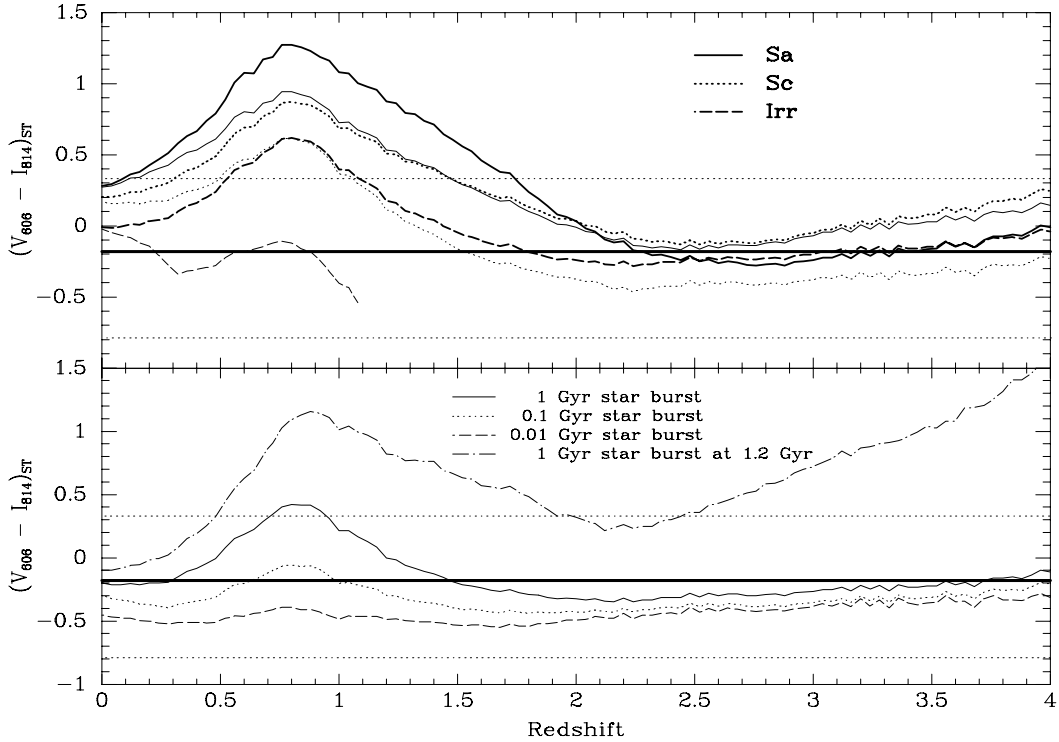


Fig. 5.— WFPC2 colors for synthesized Spectral Energy Distributions (SEDs) vs. redshift. The top panels shows the expected colors for spirals and irregular galaxies including a local extinction of $A_V = 1.19$. The thick lines include a K-correction, the thin lines include evolutionary plus K-corrections. The thick horizontal line is the best value observed color and the horizontal dotted lines its 1σ error. The bottom panel shows models of 1 Gyr (solid line), 100 Myr (dotted line) and 10 Myr (dashed line) starbursts observed at redshift z . The dot-dashed line represent a 1 Gyr starburst observed at redshift Z 200 Myr after the termination of the star formation. The truncation of the star formation with the disappearance of the most massive stars produces redder colors incompatible with the observations.

down or that the early behavior differs from the extrapolation of the later temporal behavior to earlier times, although caution is necessary when interpreting the first photometric measurements, since for example, the second point disagrees with the first and third. We believe this explanation (steady power-law decay at *late* times and uncertain photometric measurements at *early* times) is more plausible than a strong deviation from the power-law behavior at “intermediate” times, as suggested by Galama et al. (1998). The apparent shallower power-law behavior could be also a manifestation of the OT becoming redder.

What can we learn from the HST observations of the extended component? Several authors (e.g, Sahu et al. 1997c; Livio et al. 1998; Fruchter et al. 1998) have previously discussed the properties of the extended component. Fruchter et al. (1998) find that the size of the extended

component is consistent with the sizes of galaxies of comparable magnitude in the HDF. Based on this and the surface number density of galaxies of similar surface brightness, they conclude that the extended source is most likely a galaxy at moderate redshift, and is almost certainly the host galaxy of GRB970228. Here, we concentrate on the observed colors, taking into account the measured extinction, in order to constraint the nature of the likely galaxy. For that purpose, we will compare them to the colors obtained from synthetic galaxy spectra computed with PEGASE (Fioc & Rocca-Volmerange 1997), a galaxy synthesis code that reproduces the observed colors of nearby galaxies.

As mentioned before, for the extended component we measure a color of $(V_{606} - I_{814})_{ST} = -0.18^{+0.51}_{-0.61}$ in the WFPC2 images and a count-rate of 1.161 ± 0.192 in the STIS image, and we obtain a local galactic extinction of $A_V = 1.19^{+0.10}_{-0.17}$ (CL98). We prefer to use the measured color in the WFPC2 filters and the count-rate in the STIS image to avoid introducing errors in transformations to other filters. Figure 5 (top panel) presents the expected colors, including a local $R_V = 3.1$ extinction law (Cardelli et al. 1987; O’Donnell 1994) of $A_V = 1.19$, for three different spectral energy distributions corresponding to Sa (solid line), Sc (dotted line) and Irregular (dashed line) galaxies as a function of redshift, together with the observed color (solid line: best value, dotted lines: 1σ errors). We have obtained the $V_{606} - I_{814}$ color in the redshift range $0 < z < 4$ for each synthetic galaxy spectra in two ways. First, we have redshifted the spectra, which corresponds to applying a K-correction (thick lines). We have also redshifted the spectra evolving them back in time with a star forming history prescription that reproduces the observed colors at $z = 0$, which correspond to an evolutionary plus K-correction (thin lines). From Figure 5 we can check that an Sa galaxy is only consistent with our data if it is at $z \gtrsim 1.5$; an Sc, if $z \lesssim 0.4$ or $z \gtrsim 1.2$ and the constraint on irregulars depend strongly on their assumed formation time. In order to clarify what are the galaxy stellar contents allowed by the observed colors we plot in the bottom panel of Figure 5 the prediction of a 1 Gyr (solid line), a 100 Myr (dotted line) and a 10 Myr (dashed line) burst of star formation observed at redshift z at the termination of the burst. That is, the burst starts 1 Gyr, 100 Myr and 10 Myr, respectively, before it is observed at redshift z . We also show a 1 Gyr burst model that is observed at redshift z 200 Myr after the end of the burst (dot-dashed line) to understand the effect of the truncation of star formation. As Figure 5 (bottom panel) shows, on-going bursts of star formation of duration shorter than 1 Gyr produce acceptable colors; longer duration bursts begin to be unacceptable at around redshift $z \sim 0.8$. This is because, for longer duration bursts, the contribution to the total light of evolved stars increases with respect to that of the most massive stars (O and B) that are continuously formed. When the A stars start to dominate the total emitted light there is a significant flux decrement in the region of the most energetic Balmer lines (3645 – 4000 Å). This decrement passes between the F606W and F814W filters around $z \sim 0.8$, explaining the redder $V_{606} - I_{814}$ color in the bottom panel of Figure 5. Older stellar populations would produce even redder colors as late type stars contribute more and more to the integrated light (see top panel). Another important conclusion comes from the truncated star formation model (dotted-dashed line). In this case, after 200 Myr without star formation, all hot stars (O and B) have evolved off the main sequence and there is not enough ultraviolet flux to

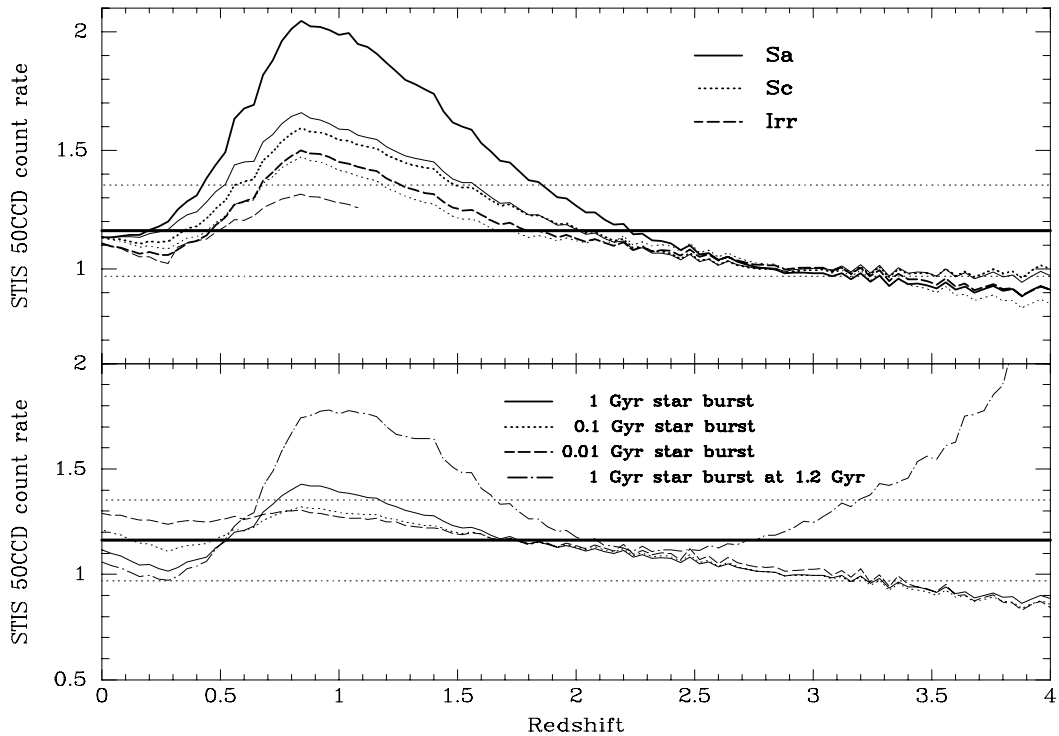


Fig. 6.— STIS count-rates for synthesized SEDs .vs. redshift. The models presented are the same as in Figure 5 but are normalized to a $(V_{606})_{ST} = 26.03$ magnitude as observed in the combined WFPC2 images.

explain the observed colors if the redshift is $z \gtrsim 0.5$.

Summarizing, the observed $V_{606} - I_{814}$ color requires the presence of hot stars dominating the ultraviolet flux if the galaxy is at $z \gtrsim 0.5$, implying on-going star formation. If the galaxy is composed of stellar populations similar to present day spirals or their likely progenitors, then its redshift is $z \gtrsim 1.2$, unless it is a dwarf at least 4 magnitudes fainter⁴ than an L^* (and semimajor axis $\lesssim 2.5h^{-1}$ kpc), in which case it could also be at $z \lesssim 0.5$, but in this case it must be unusually faint for its size.

In Figure 6 we present a similar plot, using the same synthetic spectra, but now we predict the STIS 50CCD count rate instead of the $V_{606} - I_{814}$ color. In this case, we normalize the synthetic spectra to give the observed $V_{606} = 26.03$ magnitude in the combined WFPC2 image. This only differs by 0.05 magnitudes from the V_{606} magnitudes we obtain from the measured STIS 50CCD count-rate assuming a galaxy spectrum that reproduces the color observed in the WFPC2 images

⁴Taking into account the measured local extinction

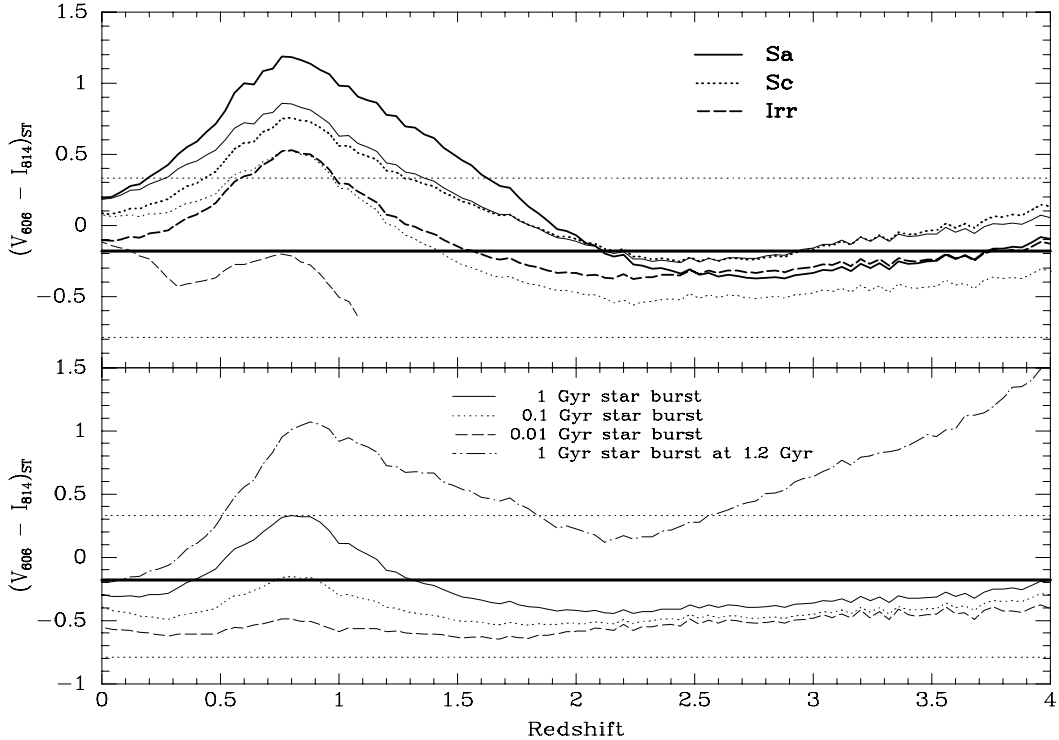


Fig. 7.— Same as figure 5, but for a local extinction of $A_V = 0.86$.

(see above and Table 2). In fact, in this way, given the wide response of the 500CCD STIS observing mode ($\sim 2000 - 10000 \text{ \AA}$), we are measuring the change in count-rate due to the change of spectral shape (or color) as we fix the normalization at V_{606} . The conclusions derived from the STIS count-rate (Figure 6) are almost the same as those derived from the WFPC2 colors. For the STIS count-rate, however, the constraint on the allowed redshift ranges for *typical* spirals are even tighter at high redshift, $z \gtrsim 1.3$. Even bursts of star formation start to have a problem explaining the measured count-rate at $z \sim 1$. We, therefore, conclude in view of the measured magnitudes and count-rate that the extended object is most likely a galaxy undergoing star formation at a redshift possibly higher than $z \sim 1.3$.

One possible source of uncertainty to our conclusion is the assumed value of the local galactic extinction. We have used the best value obtained in CL98 ($A_V = 1.19^{+0.10}_{-0.17}$), which is the result of the combination of several estimates. This value is pushed high by the extinction measured from the spectra of stars in the vicinity of GRB970228. If in CL98 we had not used the extinction estimate from the stellar spectra, we would have obtained a weighted best value of $A_V = 0.86 \pm 0.11$ (see CL98's Table 2). Figures 7 and 8 are the equivalent to Figures 5 and 6 showing the same synthesized spectra, but now for $A_V = 0.86 \pm 0.11$. As can be seen, our conclusions remain essentially unchanged.

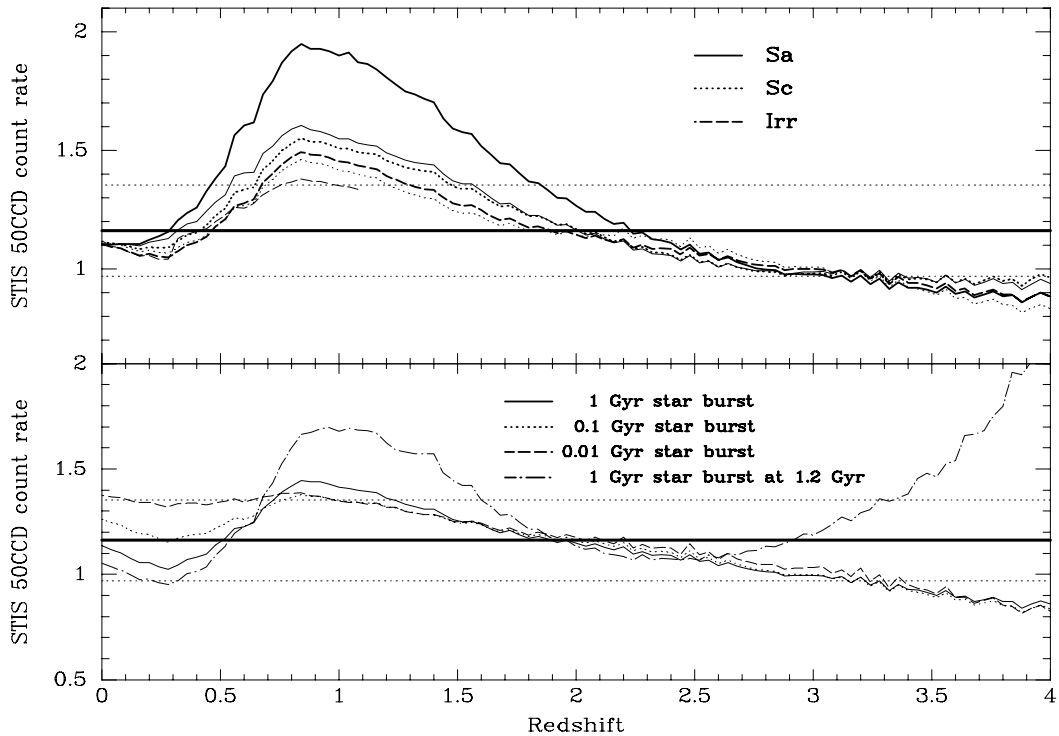


Fig. 8.— Same as figure 6, but for a local extinction of $A_V = 0.86$.

In our analyses of magnitudes and colors of the extended component so far, we have assumed no intrinsic extinction at the source. If the extended component is a galaxy with ongoing star formation, it is likely that it will contain dust and therefore absorb part of the optical radiation emitted (e.g., Calzetti et al. 1994). Should any intrinsic extinction be present, our conclusion of a galaxy with ongoing star formation would be strengthened.

Tonry et al. (1997) and Kulkarni et al. (1997) have tried to obtain the spectrum of the GRB970228 afterglow and its associated nebulosity. When the first set of observations were taken, the magnitude of the OT was similar to that of the nebulosity, while for the second set the former was significantly fainter. Neither observation revealed any obvious emission lines. If the extended source is a galaxy with ongoing star formation, strong emission lines are expected. The lack of observed [OII] and Ly α emission lines suggests that the galaxy lies at a redshift between $1.5 \lesssim z \lesssim 2.6$ for the spectral coverage of the observations, in which case the colors and size observed for the extended component would be most plausibly interpreted as those of a star forming galaxy.

4. Conclusions

We reanalyze the images of GRB970228 field taken with the HST WFPC2 and STIS instruments. Tables 1 and 2 summarize our photometric measurements. As previously reported, we find that the point source component has faded between the time elapsed by these observations while the extended component shows no significant variation. Although a possible reddening of the GRB970228 optical transient colors has been reported (Galama et al. 1998), no significant color change is detected for the point source component between the two WFPC2 images.

Analyzing the two WFPC2 images together, we find for the extended source $V_{606} = 26.03^{+0.19}_{-0.16}$ and $I_{814} = 26.21^{+0.45}_{-0.32}$, which we transform (see above) into $R_c = 25.48^{+0.22}_{-0.20}$. This magnitude is significantly fainter than that reported by Galama et al. (1998). Ground-based optical observations of the point optical transient suffered some contamination from the extended component. This contamination was negligible during the first days after the onset of the burst, but substantial after the first week. Therefore, our measured R_c magnitude implies that the total OT+extended magnitudes compiled by Galama et al. (1998) were overcorrected for the extended source by these authors in obtaining the magnitude of the OT. Using our R_c magnitude, we find that the temporal behavior of the OT is consistent with a power-law decline after the sixth day of the burst, with a temporal decay of $\alpha = -0.86 \pm 0.06$, and shows no significant deviations. The extrapolation to early epochs (before the end of the first day after the burst) would agree with the observed magnitude at Feb 28.83 UT (Guarnieri et al. 1997) but disagree with the observations at Feb 28.81 UT (Pedichini et al. 1997b) and Feb 28.99 UT (Galama et al. 1997). If we choose to fit all of the photometric points, we obtain a temporal decay slope of $\alpha = -1.04 \pm 0.03$, but the data is poorly fit, in part due to the inconsistency amongst the early measurements (see Figure 4). Given the small error bar in the WHT Feb 28.99 UT measurement and ignoring any possible zero-point error (the observation was not carried out in the R-band filter), the temporal behavior of the OT appears to have changed from a steep early decline to a shallower power-law decay after the first week. Some of this spectral slope change could be due to intrinsic reddening of the source. However, the light curve is open to multiple interpretations because the number of observations is sparse.

The WFPC2 magnitudes and STIS count-rate of the extended source component are consistent with no variation, within the errors. Several considerations indicate that this object is most likely a galaxy and possibly the host of GRB970228. If this object were a galaxy, its color, $V_{606} - I_{814} = -0.18^{+0.51}_{-0.61}$, is remarkably blue when we take into consideration the measured extinction. Using synthetic spectra we conclude that the observed emission from this object is dominated by hot stars and therefore is most likely a starburst galaxy or a spiral at high redshift. We tentatively show that its redshift is likely to be $z \gtrsim 1.2$. Further considerations of failed detection of emission lines would place this object between $1.5 \lesssim z \lesssim 2.6$.

We acknowledge valuable discussions with Daniel Reichart, Mark Metzger, Andrew Fruchter, Carlo Graziani, Jean Quashnock, Cole Miller and Dave Cole. Part of this work is based on

NASA/ESA Hubble Space Telescope archival data retrieved from the archive maintained at STScI.
We acknowledge support from NASA grants NAGW-4690, NAG 5-1454, and NAG 5-4406.

Table 1. WFPC2 Magnitudes of the GRB point and extended components.

	Point	Date	Extended	Date
V_{606}	$26.09^{+0.08}_{-0.08}$	97/03/26	$25.91^{+0.23}_{-0.19}$	97/03/26
V_{606}	$26.42^{+0.09}_{-0.10}$	97/03/26	$26.25^{+0.36}_{-0.27}$	97/04/07
I_{814}	$25.37^{+0.09}_{-0.09}$	97/04/07	$26.50^{+1.06}_{-0.52}$	97/03/26
I_{814}	$25.74^{+0.14}_{-0.11}$	97/04/07	$26.05^{+0.57}_{-0.37}$	97/04/07
V	$26.20^{+0.14}_{-0.13}$	97/03/26	$25.85^{+0.26}_{-0.23}$	Combined
R_c	$25.17^{+0.09}_{-0.08}$	97/03/26	$25.48^{+0.22}_{-0.20}$	Combined
I_c	$23.94^{+0.10}_{-0.09}$	97/03/26	$24.84^{+0.46}_{-0.42}$	Combined
V	$26.52^{+0.16}_{-0.18}$	97/04/07		
R_c	$25.52^{+0.11}_{-0.11}$	97/04/07		
I_c	$24.31^{+0.15}_{-0.11}$	97/04/07		

Table 2. STIS Magnitudes of the GRB point and extended components.

	Point	Extended
Count rate	$0.232^{+0.023}_{-0.022}$	$1.161^{+0.192}_{-0.192}$
V_{606}	$27.99^{+0.20}_{-0.18}$	$26.09^{+0.35}_{-0.24}$
I_{814}	$27.29^{+0.19}_{-0.16}$	$26.27^{+0.85}_{-0.53}$
V	$28.10^{+0.24}_{-0.23}$	$25.92^{+0.40}_{-0.27}$
R_c	$27.09^{+0.14}_{-0.14}$	$25.54^{+0.33}_{-0.22}$
I_c	$25.87^{+0.19}_{-0.16}$	$24.90^{+0.86}_{-0.63}$

Table 3. GRB afterglow point source component fit to PSF.

	F606W(03/26)	F606W(04/07)	F814W(03/26)	F814W(04/07)	STIS(09/04)
χ^2/ν	0.73	5.71	0.21	0.38	5.77

REFERENCES

- Calzetti, D., Kinney, A.L. & Storchi-Bergmann, T. 1994, *ApJ*, 429, 582
- Cardelli, J. A., Clayton, G. C. & Mathis, J. S. 1987, *ApJ*, 345, 245
- Castander, F.J. & Lamb, D.Q. 1998, *ApJ*, submitted, (CL98).
- Costa, E., Feroci, M., Frontera, F., Zavattini, G., Nicastro, L., Palazzi, E., Spoliti, G., Di Ciolo, L., Coletta, A., D'Andreta, G, et al, 1997a, *IAU Circ* 6572
- Costa, E., Feroci, M., Piro, L., Cinti, M.N., Frontera, F., Zavattini, G., Nicastro, L., Palazzi, E., Dal Fiume, D., Orlandini, M., et al, 1997b, *IAU Circ* 6576
- Djorgovski, S.G., Kulkarni, S.R., Gal, R.R., Odewahn, S.C. & Frail, D.A. 1997, *IAU Circ* 6732
- Fioc, M. & Rocca-Volmerange, B., 1997, *A&A*, 326, 950.
- Frontera, F., Greiner, J., Antonelli, L.A., Dal Fiume, D., Orlandini, M., Boller, T, Woges, W., et al, 1997, *IAUCirc* 6637
- Frontera, F., Greiner, J., Antonelli, L.A., Costa, E., Fiore, F., Parmar, A.N., Piro, L., Boller, T. & Woges, W., 1998b, *A&A*, in press, astro-ph/9804270.
- Fruchter, A., Livio, M., Macchetto, D., Petro, L., Sahu, K., Pian, E., Frontera, F., Thorsett, S. & Tavani, M., 1997, *IAU Circ* 6747
- Fruchter, A., Pian, E., Thorsett, S., González, R., Sahu, K., Mutchler, M., Frontera, F., Galama, T., Groot, P., Hook, R., Kouveliotou, C., Livio, M., Macchetto, D., van Paradijs, J., Palazzi, E., Petro, L. & Tavani, M., 1998, *Proceedings of 4th Huntsville Gamma-Ray Burst Symposium*, eds. C. A. Meegan, R. Preece, and T. Koshut, astro-ph/9801169
- Galama, T., Groot, P., van Paradijs, J., Kouveliotou, C., Robinson, C.R., Fishman, G.J., Meegan, C.A., Sahu, K.C., Livio, M., Petro, L., Macchetto, F.D., Heise, J., in't Zand, J., Strom, R.G., Telting, J., Rutten, R.G.M., Pettini, M., Tanvir, N. & Bloom, J. 1997, *Nature*, 387, 479
- Galama, T., Groot, P., van Paradijs, J., Kouveliotou, C., Sahu, K.C., Livio, M., Petro, L., Macchetto, F.D. & Fruchter, A. 1998, *Proceedings of 4th Huntsville Gamma-Ray Burst Symposium*, eds. C. A. Meegan, R. Preece, and T. Koshut, astro-ph/9712322
- Groot, P., Galama, T., van Paradijs, J., Strom, R., Telting, J., Rutten, R.G.M., Pettini, M., Tanvir, N., et al, 1997a, *IAU Circ* 6584
- Groot, P., Galama, T., van Paradijs, J., Melnick, G., van der Steene, G., Bremer, M., Tanvir, N., Bloom, J., Strom, R., Telting, J., Rutten, R.G.M., et al, 1997b, *IAU Circ* 6588

- Guarnieri, A., Bartolini, C., Masetti, N., Piccioni, A., Costa, E., Feroci, M., Frontera, F., Dal Fiume, D., Nicastro, L., Palazzi, E., Castro-Tirado, A.J. & Gorosabel, J., 1997, *A&A*, 328, L13
- Holtzman, J., Hester, J.J., Casertano, S., Trauger, J.T., Watson, A.M., Ballester, G.E., Burrows, C.J., Clarke, J.T. et al, 1995a, *PASP*, 107, 156
- Holtzman, J., Burrows, C.J., Casertano, S., Hester, J.J., Trauger, J.T., Watson, A.M. & Worthey, G. 1995b, *PASP*, 107, 1065
- Klose, S., Stecklum, B. & Tuffs, R. 1997, *IAU Circ* 6611
- Kulkarni, S.R., Djorgovski, S.G. & Clemens, 1997, *IAU Circ* 6732
- Livio, M., Sahu, K., Petro, L., Fruchter, A., Pian, E., Macchetto, D., van Paradijs, J., Kouveliotou, C., Groot, P. & Galama, T., 1998, *Proceedings of 4th Huntsville Gamma-Ray Burst Symposium*, eds. C. A. Meegan, R. Preece, and T. Koshut, astro-ph/9712097
- Margon, B., Deutch, E.W., Lamb, D.Q. & Castander, F.J. 1997, *IAU Circ* 6618
- Metzger, M.R., Kulkarni, S.R., Djorgovski, S.G., Gal, R., Steidel, C.C., 1997a, *IAU Circ* 6588
- Metzger, M.R., Cohen, J.L., Blaceslee, J.P., Kulkarni, S.R., Djorgovski, S.G., Steidel, C.C. & Frail, D.A. 1997b, *IAU Circ* 6631
- O'Donnell, J.E. 1994, *ApJ*, 422, 158
- Pedichini, F., Di Paola, A., Stella, L., Gandolfi, G., Spoliti, G., Di Ciolo, L., Coletta, A., D'Andreta, G., Muller, J.M., Capalbi, M., Boattini, A., Costa, E., Feroci, M., Piro, L., Palazzi, E., Dal Fiume, D., Nicastro, L., Frontera, F., Heise, J. & In't Zand, J. 1997, *IAU Circ* 6635
- Pedichini, F., Di Paola, A., Stella, L., Buonanno, R., Boattini, A., Gandolfi, G., Costa, E., Feroci, M., Piro, L., Dal Fiume, D., Frontera, F., Nicastro, L., Palazzi, E., Heise, J., In't Zand, J. & Vietri, M., 1997, *A&A*, 327, L32
- Reichart, D.E. 1998, *ApJ*, 485, L57
- Robinson, R.D. 1997, "Examining the STIS point spread function", http://www.stsci.edu/ftp/instrument_news/STIS/performance/psf/psf_robinson.ps
- Sahu, K. C., Livio, M., Petro, L. & Macchetto, F., 1997a, *IAU Circ* 6606
- Sahu, K. C., Livio, M., Petro, L., Macchetto, F., van Paradijs, J., Kouveliotou, C., Fishman, G. & Meegan, C., 1997b, *IAU Circ* 6619
- Sahu, K. C., Livio, M., Petro, L., Macchetto, F. D., Van Paradijs, J., Kouveliotou, C., Fishman, G. J., Meegan, C. A., Groot, P. J. & Galama, T. 1997, *Nature*, 387, 476

Soifer, B., Neugebauer, G., Armus, L., Metzger, M., Kulkarni, S., Djorgovski, S., Steidel, C. & Frail, D. 1997, IAU Circ 6619

Tonry, J. L., Hu, E. M., Cowie, L. L. & McMahon, R. G. 1997, IAUCirc 6620

van Paradijs, J., Groot, P., Galama, T., Kouveliotou, C., Strom, R.G., Telting, J., Rutten, R.G.M., Fishman, G.J., Meegan, C.A., Pettini, M., Tanvir, N., et al. 1997, Nature, 386, 686

Wijers, R.M.A.J., Rees, M.J. & Mészáros, P. 1997, MNRAS, 288, L51

Yoshida, A., Kawai, N., Otani, C., Tokanai, F., Inoue, H., Murakami, T., Nagase, F., Shibata, R., et al 1997, IAUCirc 6593